




Three-dimensional solidification modeling of various materials using the lattice Boltzmann method with an explicit enthalpy equation

Zheng Dai (代铮)¹, Zhongyi Wang (王忠义)^{1,*}, Junhao Zhu (朱俊豪)¹, Xiaohu Chen (陈小虎)^{1,†}

Qing Li (李庆)², and Zongrui Jin (金宗睿)¹

¹College of Power and Energy Engineering, *Harbin Engineering University*, Harbin 150000, China

²School of Energy Science and Engineering, *Central South University*, Changsha 410083, China



(Received 24 April 2024; accepted 9 July 2024; published 5 August 2024)

Based on the mesoscopic scale, the lattice Boltzmann method (LBM) with an enthalpy-based model represented in the form of distribution functions is widely used in the liquid-solid phase transition process of energy storage materials due to its direct and relatively accurate characterization of the presence of latent heat of solidification. However, since the enthalpy distribution function itself contains the physical properties of the material, these properties are transferred along with the enthalpy distribution function during the streaming process. This leads to deviations between the enthalpy-based model when simulating the phase transition process of different materials mixed and the actual process. To address this issue, in this paper, we construct an enthalpy-based model for different types of materials. For multiple materials, various forms of enthalpy distribution functions are employed. This method still uses the form of enthalpy distribution functions for collisions and streaming processes among the same type of substance, while for heat transfer between different materials, it avoids the direct transfer of enthalpy distribution functions and instead applies a source term to the enthalpy distribution functions, characterizing the heat transfer between different materials through the energy change before and after mixing based on the temperature. To verify the accuracy of the method proposed in this paper, a detailed solidification model for two different materials is constructed using the example of water droplets solidifying in air, and the results are compared with experimental outcomes. The results of the simulation show that the model constructed in this paper is largely in line with the actual process.

DOI: [10.1103/PhysRevE.110.025301](https://doi.org/10.1103/PhysRevE.110.025301)

I. INTRODUCTION

In various fields, particularly in nature and thermal energy systems, icing is a pervasive phenomenon. This occurrence is not limited to the icing of cables but also encompasses salt fog icing on offshore platforms, the aviation sector, crystal formation, seawater desalination, and medical applications [1–7]. Although progress has been made in the study of anti-icing at the macroscopic level, the understanding of the icing process on the surfaces of microscopic scale objects remains far from complete [8–11]. The process of pure water freezing on cold surfaces is complex, involving a variety of physical phenomena such as thermal conduction, phase transition, and the dynamic behavior of water droplets. Researchers have yet to fully reveal the details of these processes.

Liquid solidification models have been constructed at various scales. From the perspective of numerical simulation methods, they can be divided into three categories: macroscopic computational fluid dynamics (CFD) modeling based on solving the Navier-Stokes equations that assume continuity of the medium [12], the lattice Boltzmann method

(LBM) based on statistical physics theories for solving the Boltzmann equation [13], and molecular dynamics (MD) simulations based on classical Newtonian mechanics [14]. Although MD simulations, starting from the microscopic molecular motion perspective, are most capable of revealing the real solidification process, they are in practice limited by computational power, with the actual scale of simulation being several orders of magnitude smaller than the commonly used scales. The macroscopic CFD models have been successfully applied in various fields for solidification simulation, but due to their governing equations, they cannot perfectly display all phenomena and require the introduction of some empirical formulas to achieve a more perfect simulation process [15]. For example, for the commonly used enthalpy form of the energy equation, a drag source term needs to be introduced into the momentum equation to solidify the fluid, and the parameters of the mushy zone need to be adjusted according to experiments. This approach compensates for the inability to intuitively represent the solidification process from the equations and can achieve similar effects. However, this method ignores the real mechanism of icing, limiting the exploration of the mechanism of the solidification process. Based on the pseudopotential multiphase LBM proposed by Shan and Chen [16,17] (SC), subsequent scholars have made significant progress in complex flows in multiphase flow [18–22], heat transfer boiling [23–27], condensation [28], phase change of energy storage materials [29–33], etc. In using this method to

*Contact author: b205030024@126.com

†Contact author: chen_xiaohu@hrbeu.edu.cn

simulate droplet solidification, the main method comes from the enthalpy-based lattice Boltzmann (LB) models in the field of energy storage phase change [30] to solve the process of water phase change into ice in water droplets. In previous work on simulating droplet solidification, two methods were mainly used to solve the temperature field, one of which was based on a passive scalar form of temperature. However, this form has a problem in that the temperature form cannot represent latent heat issues. To solve this problem, early solutions introduced a latent heat source term in the temperature equation and used an implicit form for the solution [34], but the implicit form of the solution lost its advantage of parallel computing. To avoid implicit solving, subsequent scholars adopted a backward difference format to simplify the original form of solving the source term [35]. Based on this form, subsequent scholars constructed a droplet solidification model, including two-dimensional forms [36,37], rotating coordinate systems [13], and three-dimensional forms [38,39]. However, this simplified form of latent heat solving also caused errors in latent heat treatment, and such errors would be amplified at the solid-liquid interface [40]. Another form is the enthalpy-based model [32], which does not use a temperature distribution function form but directly uses an enthalpy distribution function form. The advantage of this form is that it can directly represent latent heat, and without needing implicit solving, it can also ensure simulation accuracy. Previous work based on this method to construct droplet solidification models was mainly for two-dimensional models [41,42]. Directly using this form to simulate droplet solidification in gas poses problems. When gas and liquid are different substances, direct transfer of enthalpy can cause deviations in the enthalpy distribution function, and this deviation will increase with the difference in physical properties between materials. This is mainly because enthalpy itself includes the physical properties of the substance, so in the streaming process of the LBM calculation, the transfer of enthalpy distribution functions between different substances, because it includes their own physical properties, will cause a significant problem of energy nonconservation.

Regarding the current state of research on LBM solidification models, there are two main issues: First, in the simulation of the solidification process, while ensuring the accurate solution of latent heat, there is a problem of energy nonconservation in the transfer of enthalpy between different substances. The second issue is the lack of a specific description of the interface between gas and solid in liquid-gas-solid solidification models. To address these two problems, in this paper, we employ the explicit enthalpy-based model to ensure the accuracy of latent heat treatment and constructs a multi-component form to avoid the energy nonconservation problem caused by the direct transfer of physical properties between different substances. This expands upon previous work and avoids the limitation of single-material models [43]. Moreover, for the liquid-gas-solid solidification model, a volume fraction parameter is introduced for detailed description, ultimately constructing a complete multicomponent solidification model.

This paper is divided into the following sections: Sec. II primarily introduces the governing equations used.

Section II A mainly discusses the governing equations for solving the flow field, while Sec. II B focuses on the governing equations used for solving the temperature field and extends them to a multicomponent form. Section III employs experimental validation to verify the proposed numerical model and specifically discusses the role of air in the solidification process. Section IV summarizes the entire paper.

II. MODELS DESCRIPTION

In this section, we first introduce the renowned SC multiphase LBM, employed for constructing a droplet and air model. Building on this foundation, we introduce an enthalpy-based LB model that considers density, extending it to the multirelaxation-time (MRT) form to ensure numerical stability. Finally, we construct a generalized enthalpy equation model from the perspectives of total enthalpy and specific enthalpy, tailored for various materials.

A. Multiphase LB model

In previous works, to achieve motion at higher Reynolds numbers (Re), the SC multiphase LBM [16] was extended from its original single-relaxation form to more stable formats such as MRT [44–46] and cascaded LBM (CLBM) [47]. Since, in this paper, we do not involve motion at high Re, we adopt the computationally less intensive MRT format [48] for a single component with the force scheme [49] as follows:

$$\begin{aligned} f_i(\mathbf{x} + \mathbf{e}_i \delta_t, t + \delta_t) - f_i(\mathbf{x}, t) \\ = -(\mathbf{M}^{-1} \mathbf{S} \mathbf{M}) [f_i(\mathbf{x}, t) - f_i^{\text{eq}}(\mathbf{x}, t)] \\ + \mathbf{M}^{-1} \left(1 - \frac{\mathbf{S}}{2}\right) \mathbf{M} \mathbf{R}_i, \end{aligned} \quad (1)$$

where f_i is the probability density distribution function, f_i^{eq} is the equilibrium probability density distribution function, \mathbf{x} is the spatial position, t is the time, δ_t is the time step, and \mathbf{e}_i is the specific direction of i direction in the velocity distribution. Here, \mathbf{R}_i represents the external force format in velocity space, and \mathbf{M} is the nonorthogonal multiple relaxation transformation matrix. The specific form of the nonorthogonal multiple relaxation transformation matrix \mathbf{M} can be referred to in previous works [22,48]. Also, \mathbf{S} is the relaxation time diagonal matrix for D3Q19 as follows [22]:

$$\begin{aligned} \mathbf{S} = \text{diag}(1, 1, 1, 1, \tau_v^{-1}, \tau_v^{-1}, \tau_v^{-1}, \tau_e^{-1}, \tau_v^{-1}, \tau_v^{-1}, \\ \tau_q^{-1}, \tau_q^{-1}, \tau_q^{-1}, \tau_q^{-1}, \tau_q^{-1}, \tau_q^{-1}, \tau_\pi^{-1}, \tau_\pi^{-1}, \tau_\pi^{-1}), \end{aligned} \quad (2)$$

where τ_e determines the bulk viscosity with the definition $\nu_b = \frac{2}{3} c_s^2 (\tau_e - 0.5) \delta_t$, τ_v determines the shear viscosity with the definition $\nu_k = c_s^2 (\tau_v - 0.5) \delta_t$, c_s is the lattice speed of sound, and τ_q and τ_π are free parameters.

During the solidification process, as the fluid transitions to a solid, the gray LB equation (GLBE) method [50] is utilized to more accurately characterize the flow state throughout the droplet freezing process. In this approach, the mixture of solid and liquid during the phase transition is considered a porous medium, allowing the flow process to be modified

as follows:

$$f_i(\mathbf{x} + \mathbf{e}_i \delta_t, t + \delta_t) = f_i f_i^*(\mathbf{x}, t) + (1 - f_i) f_i^*(\mathbf{x} + \mathbf{e}_i \delta_t, t), \quad (3)$$

where f_l represents the liquid phase fraction, in which $f_l = 1$ represents the liquid phase fraction, and $f_l = 0$ indicates a solid phase region, and values between 0 and 1 correspond to a solid-liquid mixture area. Here, f_i^* is the postcollision distribution function, and \bar{i} denotes the distribution function in the direction opposite to i .

In the pseudopotential model, an interaction force between fluids [13,39] is introduced to achieve spontaneous phase separation. To realize a higher density ratio, in this paper, we utilize a modified combination of pseudopotential forces [21], specifically defined as

$$\mathbf{F}_m = -\lambda G \sum_i w(|\mathbf{e}_i|^2) \psi(\mathbf{x} + \mathbf{e}_i \delta_t)^2 \mathbf{e}_i - (1 - 2\lambda) G \psi(\mathbf{x}) \times \sum_i w(|\mathbf{e}_i|^2) \psi(\mathbf{x} + \mathbf{e}_i \delta_t) \mathbf{e}_i, \quad (4)$$

where $G = -1$ represents the interaction strength, $w(|\mathbf{e}_i|^2)$ are the weights, with specific weights for D3Q19 being $w(1) = \frac{1}{6}$, $w(2) = \frac{1}{12}$, and ψ is the effective mass. Following the work of Yuan and Schaefer [51], the effective mass $\psi(\mathbf{x})$ suitable for any nonideal gas state equation is

$$\psi(\mathbf{x}) = \sqrt{\frac{2(P_{\text{EOS}} - \rho c_s^2)}{G c^2}}, \quad (5)$$

where P_{EOS} is the nonideal gas state equation. To simulate air and water components under a single component model, in this paper, we adopt the linear form equation of state (EOS) [52], a method that has been used multiple times in previous works [21,52–54], the details of which are not elaborated here. The specific formula is as follows:

$$P_{\text{EOS}} = \begin{cases} \rho \theta_g, & \rho < \rho_1, \\ \rho_1 \theta_g + (\rho - \rho_1) \theta_m, & \rho_1 < \rho < \rho_2, \\ \rho_1 \theta_g + (\rho_2 - \rho_1) \theta_m + (\rho - \rho_2) \theta_l, & \rho_2 < \rho. \end{cases} \quad (6)$$

Regarding parameter settings, in previous works [21], $\rho_l = 1$ and $\rho_v = 0.001$, with a kinematic viscosity ratio of 20 between the gas and liquid phases. To achieve a more realistic gas-liquid restoration, in this paper, we use a density ratio closer to real conditions, referencing the properties of water and air at 0°C, with postequilibrium gas and liquid density values set to $\rho_l = 1$ and $\rho_v = 0.00125$, and the gas and liquid kinematic viscosity ratio set to 7.5. To ensure correct evolution of the droplet interface, the liquid-gas interface thickness is maintained at 5 lattices [52,55], with parameter settings of $\theta_g = 0.5c_s^2$, $\theta_l = c_s^2$, and $\theta_m = -0.03c_s^2$. The values of $\rho_1 = 0.001724$ and $\rho_2 = 0.9712$ are calculated using the Maxwell equal area method. To ensure thermodynamic consistency, λ is set to -0.713 .

In this paper, the fluid-solid interaction force \mathbf{F}_{ads} is defined to simulate the adhesive force between the fluid and the solid [56], and weighted average density of ghost fluid nodes ρ_{ghost} close to solid boundary [57], which are given by

$$\mathbf{F}_{\text{ads}} = -G_w \psi(\mathbf{x}) \sum_i w_i(|\mathbf{e}_i|^2) \psi(\mathbf{x}) s(\mathbf{x} + \mathbf{e}_i \delta_t) \mathbf{e}_i, \quad (7)$$

$$\rho_{\text{ghost}} = \frac{\sum_i \omega_i \rho(\mathbf{x} + \mathbf{e}_i \delta_t) [1 - s(\mathbf{x} + \mathbf{e}_i \delta_t)]}{\sum_i \omega_i [1 - s(\mathbf{x} + \mathbf{e}_i \delta_t)]}, \quad (8)$$

where G_w is the fluid-solid interaction strength to adjust the droplet contact angle, s is an indicator function which is equal to 1 for solid and 0 for fluid, and ω_i is the weight of D3Q19. The resultant force is defined as $\mathbf{F} = \mathbf{F}_m + \mathbf{F}_{\text{ads}} + \mathbf{F}_g$, and \mathbf{F}_g is the body force, such as gravity.

B. Modeling of various materials with enthalpy-based model

The energy equation in enthalpy form is widely used to solve the solidification process. Compared with the temperature form, the enthalpy form can consider the latent heat released by water during solidification. When simulating water solidification, viscosity dissipation terms are typically neglected, and for a stationary liquid droplet, it can be treated as an incompressible fluid. The macroscopic enthalpy equation can be expressed as follows:

$$\frac{\partial(\rho H)}{\partial t} + \nabla \cdot (\rho \mathbf{v} H) = \nabla \cdot (\lambda \nabla T), \quad (9)$$

where ρ is the macroscopic density of the current node, H is the total enthalpy of the current node, λ is the thermal conductivity of the current node, \mathbf{v} is the macroscopic velocity, and T is the temperature of the current node. In this paper, due to variations in density and specific heat capacity, we cannot rely on previous approaches that only consider changes in specific heat. In previous work [43], it was possible to decouple density and specific heat without considering thermal convection. For our current investigation, in which we focus on stationary water droplets, we adopt this method to ensure accurate recovery of density and specific heat properties between air and water. To prevent the transfer of enthalpy containing physical properties between different substances, in this paper, we construct a multicomponent form with the MRT format for the collision process as follows:

$$h_i^{k,*}(\mathbf{x}, t) = h_i^k(\mathbf{x}, t) - (\mathbf{N}^{-1} \mathbf{\Gamma} \mathbf{N}) [h_i^k(\mathbf{x}, t) - h_i^{k,\text{eq}}(\mathbf{x}, t)], \quad (10)$$

where h_i^k is the probability enthalpy distribution function for the k component, $h_i^{k,\text{eq}}$ is the equilibrium probability enthalpy distribution function, and \mathbf{N} is the orthogonal multiple relaxation transformation matrix [32].

Here, $\mathbf{\Gamma}$ is the relaxation time diagonal matrix for the D3Q7 model as follows:

$$\mathbf{\Gamma} = \text{diag}(\sigma_0, \sigma_1, \sigma_2, \sigma_3, \sigma_4, \sigma_5, \sigma_6), \quad (11)$$

where $\sigma_1 = \sigma_2 = \sigma_3 = \sigma_\chi$, with σ_χ determining the thermal diffusivity $\chi = (\frac{1}{\sigma_\chi} - \frac{1}{2}) c_{sT}^2 \delta_t$. It is important to note that, to avoid numerical diffusion near the solid-liquid interface [32], it is necessary to satisfy $\sigma_1 + \sigma_4 = 2$. The equilibrium enthalpy distribution function under the MRT format can be

defined as

$$\mathbf{N}^{k,\text{eq}} = \mathbf{N} \mathbf{h}_i^{k,\text{eq}} = (\rho_f^k H^k, 0, 0, 0, 6\rho_f^k H^k - 21\omega_T \rho_{\text{ref}}^k C_{p,\text{ref}}^k T, 0, 0)^T, \quad (12)$$

where ρ_{ref}^k , $C_{p,\text{ref}}^k$ are the reference density and reference specific heat capacity at constant pressure, respectively.

For the streaming process, the concept of component fraction ξ^k is introduced, drawing on the GLBE method. In this context, during the streaming process, the fraction ξ^k is effective, while the fraction $1 - \xi^k$ is ineffective. Furthermore, heat transfer between components is introduced in the form of a source term:

$$\begin{aligned} h_i^k(\mathbf{x} + \mathbf{e}_i \delta_t, t + \delta_t) &= \xi^k h_i^{k,*}(\mathbf{x}, t) + (1 - \xi^k) h_i^{k,*}(\mathbf{x} + \mathbf{e}_i \delta_t, t) \\ &+ \mathbf{N}^{-1} \left(1 - \frac{\Gamma}{2} \right) \mathbf{N} \xi^k \tilde{Q}_i^k(\mathbf{x} + \mathbf{e}_i \delta_t, t), \end{aligned} \quad (13)$$

where Q_i^k represents the heat received by a component from the rest, signifying the energy exchange between different components. In this paper, it is assumed that, at a given node

within a multicomponent system, different components, after being sufficiently mixed, reach a uniform temperature. This involves the transient response of each component, transitioning from its original state (its temperature unaffected by other components) to the temperature after mixing. During this process, the energy exchange between different components is considered a source term, reflected in the enthalpy distribution function of each component. Following the introduction of the thermal source form [58], the macroscopic parameter update is modified to $\rho_f^k H^k = \sum_{i=0}^{m-1} h_i^k + \frac{\xi^k Q_i^k}{2}$, where ρ_f^k is defined by the density values before and after the phase change, i.e., $\rho_f^k = f_l^k \rho_l^k + (1 - f_l^k) \rho_s^k$. The specific form of the source term is

$$Q_i^k = \omega_i \rho_f^k C_p^k (T - T^k), \quad (14)$$

where ω_i represents the weight of the enthalpy distribution function in different directions, ρ_f^k is the mass fraction of the k component at the current lattice point, with $\sum_{k=1}^n \xi^k = 1$, T^k is the temperature of the k component before sufficient mixing, and T is the uniform temperature reached after sufficient mixing of different components. The temperature T^k before sufficient mixing is defined as follows:

$$T^k = \begin{cases} \frac{\rho_f^k H^k}{\rho_s^k C_{p,s}^k}, & \rho_f^k H^k < \rho_s^k H_s^k, \\ T_s^k + \frac{\rho_f^k H^k - \rho_s^k H_s^k}{\rho_f^k H_l^k - \rho_s^k H_s^k} (T_l^k - T_s^k), & \rho_s^k H_s^k \leq \rho_f^k H^k \leq \rho_l^k H_l^k, \\ T_l^k + \frac{\rho_f^k H^k - \rho_l^k H_l^k}{\rho_l^k C_{p,l}^k}, & \rho_f^k H^k \geq \rho_l^k H_l^k, \end{cases} \quad (15)$$

where T_l^k is the temperature when the k component solid completely melts into liquid, T_s^k is the temperature when the k component solid starts to melt, H_l^k is the enthalpy when the k component solid completely melts into liquid, and H_s^k is the enthalpy when the k component solid starts to melt. The temperature T for different components after sufficient mixing and the introduction of latent heat is more complex and is elaborated in the following section.

It is important to note that, typically, the source term should be added during the collision process. However, to ensure that the thermal source term acts entirely on the

effective part and not on the ineffective part, it needs to be incorporated during the streaming process. Inclusion during streaming requires consideration of the migration of the thermal source term. During the migration process, there is a distinction between the gradient of the component fraction in the forward direction and the gradient in the reverse direction. In the case of the reverse component fraction gradient, excess thermal sources are reflected to fill the gaps in the forward component fraction gradient. Based on these considerations, the thermal source term in the streaming process is as follows:

$$\tilde{Q}_i^k(\mathbf{x} + \mathbf{e}_i \delta_t, t) = \begin{cases} \xi^k(\mathbf{x} + \mathbf{e}_i \delta_t, t) Q_i^k(\mathbf{x}, t), & \xi^k(\mathbf{x}, t) \leq \xi^k(\mathbf{x} + \mathbf{e}_i \delta_t, t), \\ [\xi^k(\mathbf{x} + \mathbf{e}_i \delta_t, t) - \xi^k(\mathbf{x}, t)] Q_i^k(\mathbf{x}, t) + \xi^k(\mathbf{x}, t) Q_i^k(\mathbf{x}, t), & \xi^k(\mathbf{x}, t) > \xi^k(\mathbf{x} + \mathbf{e}_i \delta_t, t), \end{cases} \quad (16)$$

where considering the spatial variation of the component fraction ensures accuracy in cases where the component fraction is not constant.

III. CONSTRUCTION AND VALIDATION OF WATER FREEZING MODEL IN AIR

To provide a more detailed description of the multicomponent solidification model, in this section, we focus on

constructing a liquid-gas biphasic solidification model based on air and water. Initially, a more specific explanation of the formulas applied in the second part of this paper is provided, supplementing the details required for the liquid biphasic solidification model. Finally, the completed liquid-gas solidification model is applied and compared with experimental results to verify the accuracy of the model presented in this paper.

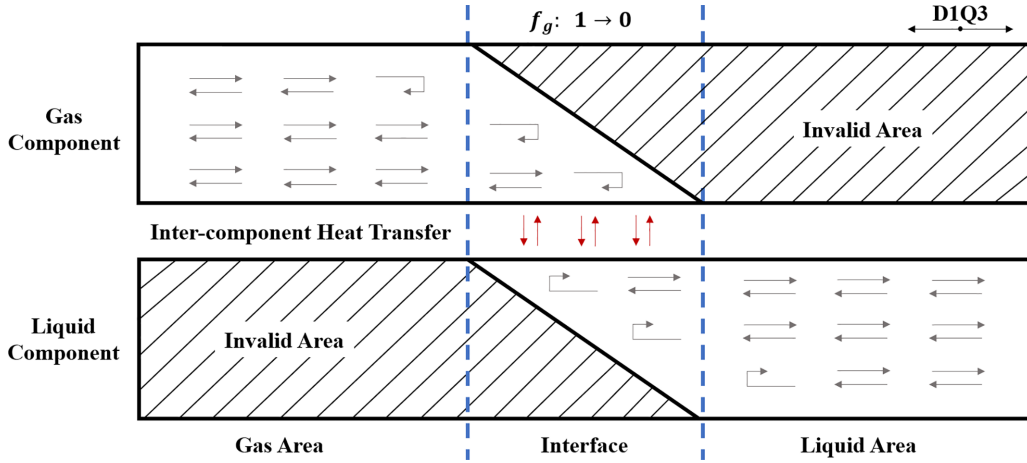


FIG. 1. Schematic of the distribution function transfer within and between liquid-gas two-component phases in D1Q3 (gray arrows represent the transfer process of the enthalpy distribution function for each component, red arrows indicate the process of temperature transfer between components, and the invalid areas are parts where no energy transfer occurs).

A. Construction of liquid-gas two-component model

Previous work [41,59] employed a single-component enthalpy-based model to describe the solidification process of water in air. However, this method has certain limitations in handling energy conservation because it relies on the form of the enthalpy-temperature equation. Specifically, for liquid water, its enthalpy mathematical expression can be defined as $H_l(T) = C_{p,l}(T - T_l) + C_{p,s}T_s + \Delta H_{l,s}$, where for water $T_l = T_s$, and $\Delta H_{l,s}$ represents the latent heat of solidification for water. For air, the enthalpy can be defined as $H_g(T) = C_{p,g}T$. The enthalpy expressions for both substances at the same temperature include their respective physical parameters. Regarding the enthalpy distribution function, the sum of its directions equals $\rho_f^k H^k = \sum_{i=0}^{m-1} h_i^k$, indicating that the enthalpy distribution function is a function of its density, specific heat capacity, and temperature, specifically expressed as

$$h_i^k = f(\rho_f^k, C_p^k, T). \quad (17)$$

For the process of solving, the enthalpy distribution function during the streaming process [43] is as follows:

$$h_i^k(\mathbf{x} + \mathbf{e}_i \delta_t, t + \delta_t) = h_i^{k,*}(\mathbf{x}, t). \quad (18)$$

At the liquid-gas interface during this process, the gas transfers its distribution function, containing its specific heat capacity and density physical parameters, to the liquid and vice versa. This leads to confusion in heat transfer at the interface, causing energy nonconservation. The multicomponent form can avoid this issue.

To provide a more detailed description of the distribution function transfer within a multicomponent system, in this paper, we introduce the concept of gas fraction, which is the air fraction at a given node, specifically defined as

$$f_g = \frac{\rho_l - \rho}{\rho_l - \rho_g}, \quad (19)$$

where ρ is the density at the current node. At 0 °C, the air dissolved in water can be considered negligible; therefore, we

assume that the air part contains no water, i.e., $f_g = 1$, and the water part contains no air, i.e., $f_g = 0$.

In the liquid-gas multicomponent system, the liquid component in the gas region is defined as the invalid area of the liquid component, and likewise, the gas component in the liquid region is considered an invalid area. During the process of distribution function transfer, if the next node contains an invalid area, the invalid part of this node is reflected, as specifically illustrated in Eq. (13). This approach is like the GLBE method [50] used within fluid domains. Heat transfer between components is implemented in the form of a source term acting on the enthalpy distribution function, effectively avoiding the issue of transferring physical properties. For a more intuitive representation, we use D1Q3 (one dimension, three directions) for a simple illustration in Fig. 1.

For the solidification process of water, the concept of liquid fraction is used to differentiate between water and ice, with its value determined by the enthalpy, specifically defined [43] as follows:

$$f_l = \begin{cases} 0, & \rho_f H \leq \rho_s H_s, \\ \frac{\rho_f H - \rho_s H_s}{\rho_l H_l - \rho_s H_s}, & \rho_s H_s < \rho_f H < \rho_l H_l, \\ 1, & \rho_l H_l \leq \rho_f H. \end{cases} \quad (20)$$

At 0 °C, the proportion of water vapor in air and air in water is very low, so in this paper, we neglect the presence of air in water and water vapor in air. In the entire model of a water droplet solidifying in air, it is divided into seven regions, namely: the gas zone, liquid zone, solid zone, gas-liquid interface zone, liquid-solid mushy zone, gas-liquid-solid zone, and gas-solid zone. The specific proportions of these regions are illustrated in Fig. 2. It is important to note that, although the computational domain is divided into three main areas—gas, liquid, and solid—it remains a two-component system of air and water, with liquid water and solid ice included within the water component. The concept of liquid fraction primarily originates from previous studies [32], mainly acting within the water component and not affecting the air component.

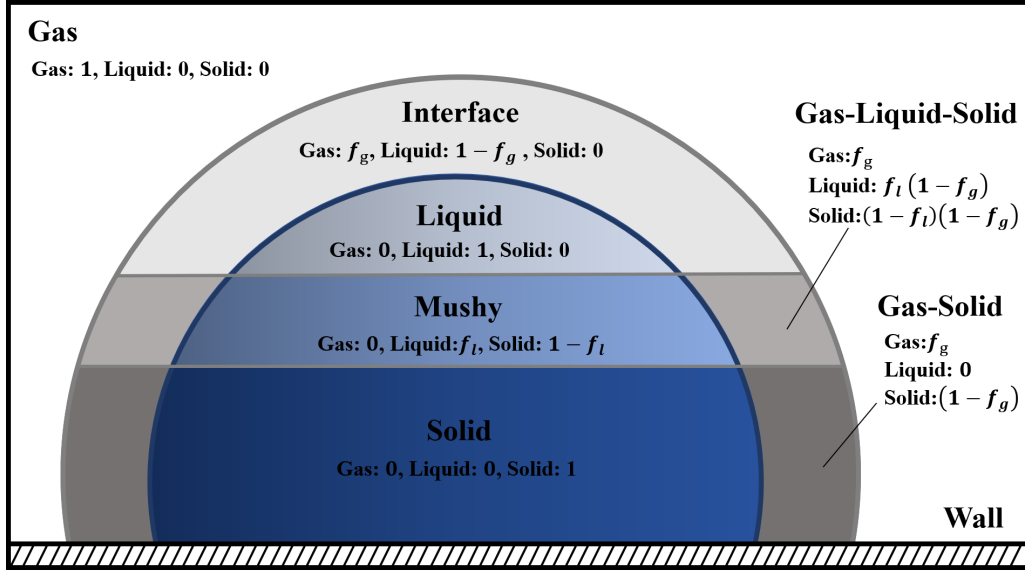


FIG. 2. Schematic of the liquid-gas two-component solidification model (gas zone: area where only gas exists; liquid zone: area where only liquid exists; solid zone: area where only solid exists; gas-liquid interface zone: intersection where gas and liquid mix; liquid-solid mushy zone: coexistence area of liquid and its solid form; gas-liquid-solid zone: intersection where liquid and its solid form coexist with gas; and gas-solid zone: intersection of the completely solidified part of the liquid with gas).

Based on the introduction of the gas fraction concept, the total enthalpy of the two components, gas and liquid, is defined as

$$\rho_f H = f_g \rho_g H_g + (1 - f_g) \rho_l H_l, \quad (21)$$

where ρ_g is the density of air, which does not undergo density changes due to phase transitions, and thus the density of the air part is unaffected by the liquid fraction. Based on Eq. (21), the temperature T of air and water when fully mixed can be derived with the specific formula:

$$T = \begin{cases} \frac{\rho_f H}{f_g \rho_g C_{p,g} + (1 - f_g) \rho_s C_{p,s}}, & \rho_f H \leq f_g \rho_g C_{p,g} T_s + (1 - f_g) \rho_s H_s, \\ T_s + \frac{\rho_f H - (f_g \rho_g C_{p,g} T_s + (1 - f_g) \rho_s H_s)}{f_g \rho_g C_{p,g} T_l + (1 - f_g) \rho_l H_l - (f_g \rho_g C_{p,g} T_s + (1 - f_g) \rho_s H_s)} (T_l - T_s), & f_g \rho_g C_{p,g} T_s + (1 - f_g) \rho_s H_s < \rho_f H < f_g \rho_g C_{p,g} T_l + (1 - f_g) \rho_l H_l, \\ \frac{\rho_f H - (1 - f_g) (\rho_l H_l - \rho_l C_{p,l} T_l)}{f_g \rho_g C_{p,g} + (1 - f_g) \rho_l C_{p,l}}, & f_g \rho_g C_{p,g} T_l + (1 - f_g) \rho_l H_l \leq \rho_f H. \end{cases} \quad (22)$$

The temperature before full mixing is the same as defined in Eq. (15).

Before proceeding with numerical validation, it is necessary to construct the computational domain. The size of the computational domain is $200 \times 200 \times 120$, with a hemispherical droplet of 50 l.u. radius initialized at the center of the wall, which is equivalent to a spherical droplet with a radius of 40 l.u. based on volume conversion. For the flow field boundary conditions, the top and bottom boundaries use the halfway bounce-back boundary condition, while the rest employ periodic boundary conditions. Regarding the temperature field boundary conditions, the bottom boundary is set with a constant temperature boundary condition, and the rest use the fully developed boundary condition, as illustrated in Fig. 3. In the initialization part, only the flow field is simulated to prevent fluctuations during initialization from affecting the temperature field.

B. Validation of liquid-gas two-component model

To accurately simulate the solidification process of air in water, it is necessary to precisely introduce the physical properties of air and water. In previous studies, although the physical properties of water have been accurately restored, the physical properties of air have rarely been considered with precision. Especially in terms of the critical parameter of density ratio, past researchers often did not use real density ratio values. This approach, without accurately introducing air density, inevitably leads to deviations in other physical properties relative to air to make simulation results closer to reality. This causes the simulation of the air part to lack reference significance.

To address this issue, the main challenge we face originates from the drastic changes in density and thermal conductivity at the phase transition interface. Such significant changes in physical properties, especially in the LB simulations of

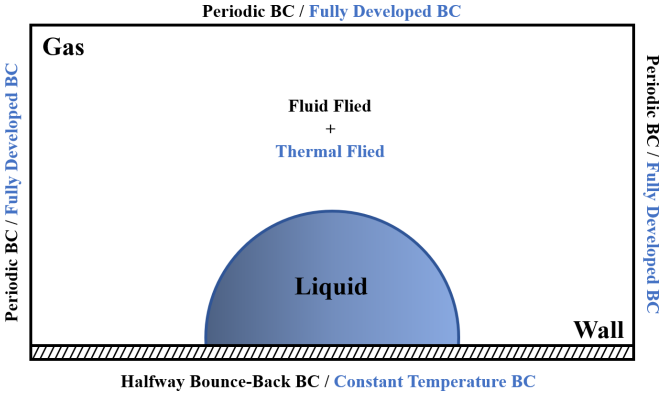


FIG. 3. Front view of the computational domain (black font: flow field boundary conditions; blue font: enthalpy equation boundary conditions).

continuous phase interfaces, present considerable technical difficulties. In the enthalpy-based model, the sudden shifts in physical properties directly lead to decisive changes in thermal diffusivity, thereby affecting the setting of relaxation times. Under conditions at 0 °C, the thermal diffusivity of air is 143 times higher than that of water, which theoretically should mean that heat transfer in air is much faster than in water. However, in previous studies using the same method, observed changes in the temperature field did not reflect a faster decrease in air temperature than water. This finding challenges our understanding of the heat transfer process and points to potential areas for improvement in handling these abrupt changes in physical properties within the model.

To compare with experimental setups, we selected the following dimensionless numbers:

$$\begin{aligned} \text{Bo} &= \frac{gR^2(\rho_l - \rho_g)}{\sigma}, & \text{Pr} &= \frac{\mu_l C_{p,l}}{\lambda_l}, \\ \text{St} &= \frac{C_{p,l}(T_f - T_w)}{\Delta H_{ls}}, & \text{Fo} &= \frac{\lambda_l t}{\rho_l C_{p,l} R^2}. \end{aligned} \quad (23)$$

Within the constraints of these dimensionless numbers, the parameters of water were restored. To achieve the restoration of the physical parameters of air and ice, we restricted the ratios of the physical parameters of air, ice, and water. We set the specific heat capacities of air, ice, and water as 1:2:4, matching the actual ratios at 0 °C, with specific values set as

$C_{p,g} = 0.25$, $C_{p,s} = 0.5$, and $C_{p,l} = 1$. For the setting of thermal diffusivity, in this paper, we calculate using the following:

$$\frac{f_g \lambda_g + (1 - f_g)[f_l \lambda_l - (1 - f_l) \lambda_s]}{f_g \rho_g C_{p,g} + (1 - f_g)(\rho_{\text{ref}} C_{p,\text{ref}})} = \left(\frac{1}{\sigma_x} - \frac{1}{2} \right) c_{sT}^2 \delta_t, \quad (24)$$

where the thermal conductivities are set to $\lambda_g = 0.000309$, $\lambda_s = 0.0297$, and $\lambda_l = 0.00731$.

Ensuring the same dimensionless numbers as in the experiments: $\text{Bo} = 0.265$, $\text{Pr} = 13.679$, and $\text{St} = 0.19$, and the droplet contact angle $\theta = 103^\circ$, since the Stefan number St includes the wall temperature and the freezing point temperature of liquid but not the initial droplet temperature, to ensure the accuracy of parameter settings, we calibrated the initial droplet temperature using an infrared camera. We fixed the ratio of the temperature difference between the initial droplet and the freezing point to the ratio of the wall temperature and the freezing point temperature, applying it in the numerical simulation to ensure the correctness of the parameter settings. In this paper, we aim to compare the morphologies under different Fourier numbers Fo . In defining the outer contour of the droplet, we selected the isosurface with a density value of 0.5 as the criterion.

In Fig. 4, we compare the cross-section at the exact center of the droplet during the numerical simulation process with the outer contour of the droplet from the experiment, using the Fourier number Fo as the dimensionless time axis. The black dashed line in the simulation results and the red dashed line in the experimental results represent the growth peak of the droplet. The growth of the ice peak during the freezing process essentially matches.

To deeply analyze and accurately compare the differences between simulation results and experimental data, we utilized the dimensionless number Fo as a benchmark for comparison, focusing on the dynamic changes of two key parameters: phase interface height and relative radius, as shown in Fig. 5. We observed that, to the left of the time point marked by the red dashed line, the simulation results closely match the experimental data. However, to the right of this time point, we found that the maximum value of the phase interface height and the minimum value of the relative radius in the simulation results appear earlier than in the experimental results. Nonetheless, the end time of droplet freezing in the simulation is consistent with the end time in the experiment. It is worth noting that, in previous work [13,59], the volume change

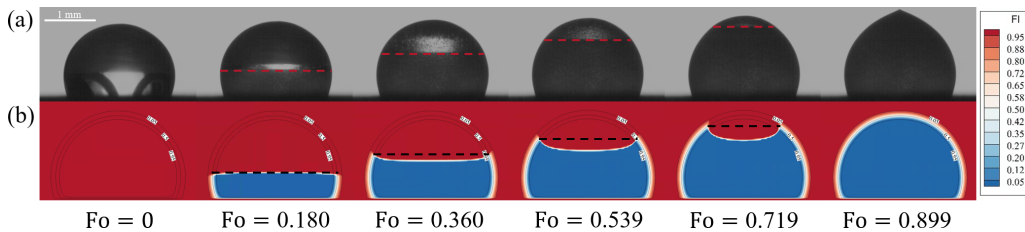


FIG. 4. Comparison of the droplet freezing process in simulation experiments (a) the droplet diameter is 2.8 mm, the droplet temperature is 8.5 °C, the ambient temperature is 8 °C, the wall temperature is consistently maintained at −15 °C, and the atmospheric pressure is at standard atmospheric pressure. The specific testing methods are referenced in the appendix. (b) The simulation uses isosurfaces where the liquid fraction is 0.5 or the density value is 0.5 to differentiate between the gas phase and the liquid phase (solid phase).

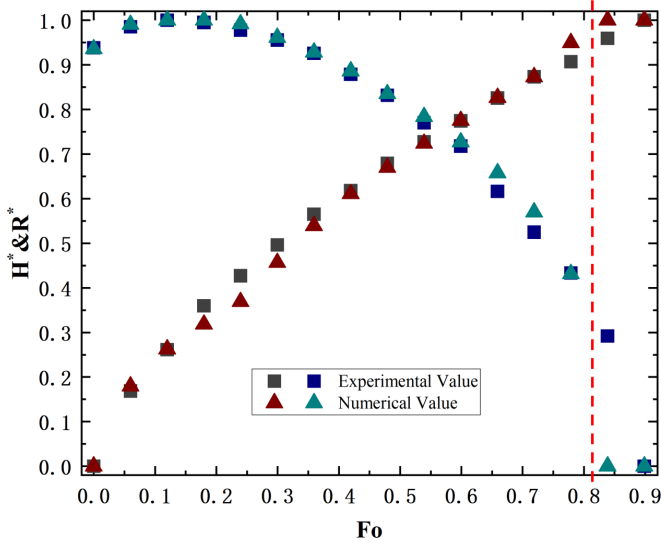


FIG. 5. Comparison of phase interface height and relative radius between simulation and experiment (the red line distinguishes between areas that conform to and do not conform to experimental controls).

process of water freezing into ice was achieved through mass sources. However, their work was conducted using a two-dimensional axisymmetric system. To ensure the simulation results matched experimental data, they set the droplet radius to 100 l.u., which requires an enormous computational effort to simulate static droplet freezing in three-dimensional (3D) conditions. For droplets of this size, the volume change during the later stages of the solidification process is accurately represented due to the small cross-sectional area of the droplet. In

this paper, we use a 3D model. If we used droplets of the same size, the computational load and time would be unacceptable. For our simulated droplet size (lattice radius of 40 l.u.), the entire computational domain contains 4.8 million lattice points and requires 200 000 steps to complete the process, taking nearly a day of parallel computation on our GPU device (Nvidia A40). We estimate that, for our computational domain ($5R \times 5R \times 3R$), the grid count would reach 75 million, increasing the computational load by >15 times. Moreover, to match the experimental $Fo = \frac{\lambda_l t}{\rho_l C_{p,l} R^2}$, the required time steps are proportional to the square of the droplet radius, meaning we would need to compute 1.3 million time steps. This results in a nearly 100-fold increase in computational load, which is enormous. Without considering droplet volume changes, significant deviations in droplet shape during the last 10% of the solidification process only start to appear in Fig. 6.

Furthermore, to investigate the reasons behind the significant deviations between simulation and experimental results within the Fourier number range from 0.779 to 0.899, we conducted a detailed comparison of the temperature and solid fields within this interval, as shown in Fig. 6. A notable finding is that, influenced by the continuous exposure to cold air, the sides of the droplet begin to freeze before the center does. Just before solidification completes, the outer ice peaks envelop the droplet first, leading to the phenomenon of ice growth toward the inside of the droplet. This simulation result explains why the maximum value of the phase interface height and the minimum value of the relative radius are reached first in the simulation, even though the actual solidification process has not yet been completed. This indicates that, although the droplet shape deviates from the experimental results just before complete solidification, the solidification time still matches the experiment.

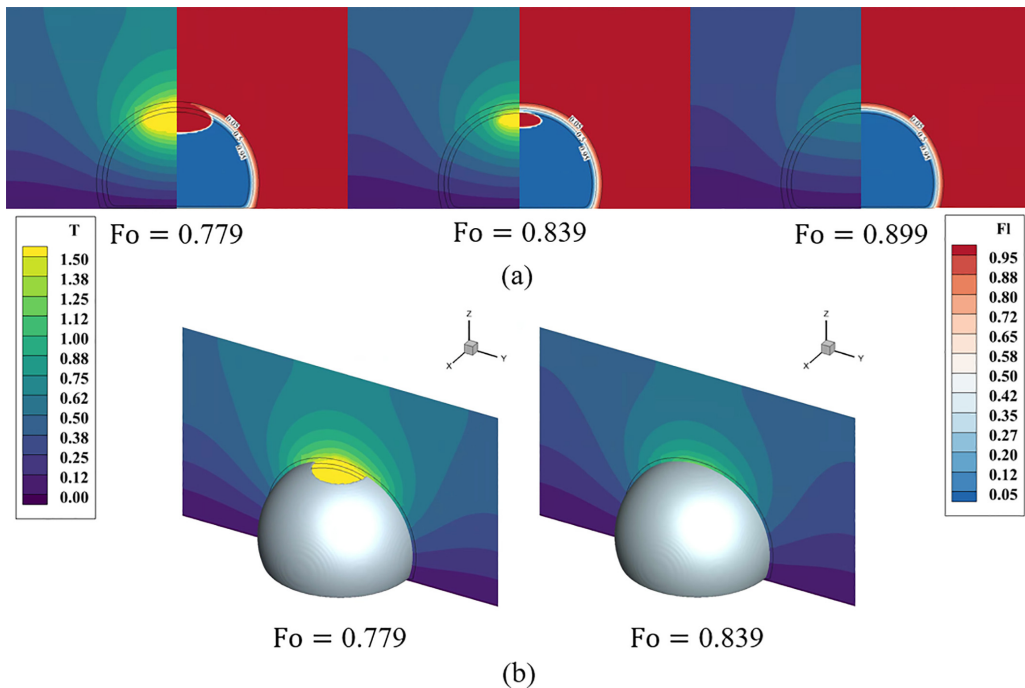


FIG. 6. (a) Comparison of the temperature field (left) and solidification field (right) just before the end of solidification. (b) Three-dimensional perspective.

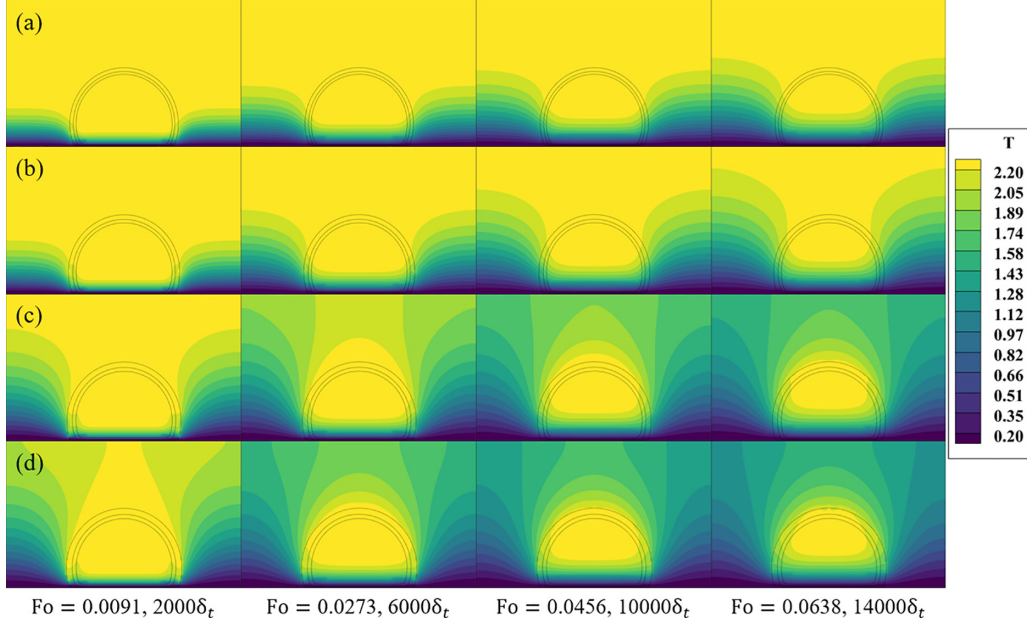


FIG. 7. Under the same conditions of specific heat at constant pressure and thermal conductivity, temperature transfer for different liquid-gas density ratios ($T = 1.5$ is the freezing point) (a) $\rho_l/\rho_g = 40$, $\chi_l/\chi_g = 7.179$, (b) $\rho_l/\rho_g = 80$, $\chi_l/\chi_g = 14.357$, (c) $\rho_l/\rho_g = 400$, $\chi_l/\chi_g = 71.787$, and (d) $\rho_l/\rho_g = 800$, $\chi_l/\chi_g = 143.574$.

We compared the temperature diffusion cloud diagrams for different liquid-gas density ratios (with linear EOS parameters set as $\theta_g = 0.5c_s^2$, $\theta_l = c_s^2$, and $\theta_m = -0.03c_s^2$, for each density ratio, calculating respective ρ_1 , ρ_2 and adjusting λ to ensure thermodynamic consistency) in Fig. 7. For other parameters, we adhered to the physical properties of water and air. In real environments (at 0°C), the thermal diffusivity of air is 143 times that of water, as shown in Fig. 7(d). In previous work, the commonly used liquid-gas density ratio is ~ 40 . Authors of previous studies [13,59] used the Peng Robinson EOS to represent water and air, with parameters $T/T_c = 0.8$, resulting in a liquid-gas density ratio of ~ 36 at this temperature. It is evident that, when $\rho_l/\rho_g = 800$, within a very short time (Fo at the end of solidification is 0.899), which is $\sim 1\%$ of the total solidification time, the cold air rapidly envelops the droplet. However, when $\rho_l/\rho_g = 40$ and 80 , the air temperature does not fully envelop the droplet even in the first 10% of the total solidification time.

To specifically analyze the heat transfer process between air and water under actual conditions, we have illustrated a schematic diagram in Fig. 8. In fact, although the thermal diffusivity of air is much higher than that of water, the droplet is not significantly affected by the rapid cooling of the air. This is because the density and specific heat capacity of water are both greater than those of air ($\rho_l C_{p,l}/\rho_g C_{p,g} \approx 3200$). The large disparity in physical properties means that when the droplet is enveloped by cold air, only the ice peak at the air-water-ice triple line gradually rises higher than the ice peak at the center of the droplet over time.

To further deepen the understanding of the extent to which air affects the solidification process of pure water droplets, in this paper, we employed a quantitative analysis method based on these simulation results. By analyzing the solidification growth rates at the periphery and the center of the

droplet during the solidification process in detail, we observed key characteristics of the solidification dynamics. Specifically, from the data comparison in Fig. 9, we identified that, in the initial stages of solidification, the solidification growth rate inside the droplet, whether hydrophilic or hydrophobic, is significantly faster than on the outside. This phenomenon is manifested in the 3D solid reconstruction images as an initial protrusion in the center of the droplet. As time progresses, the influence of the surrounding cold air on the droplet gradually becomes significant, leading to the solidification growth height on the outside of the droplet exceeding the inside and increasing at an almost constant rate, eventually surpassing the internal growth rate to reach a peak. During this process, the solid phase structure inside the droplet undergoes a morphological change from protrusion to concavity.

IV. CONCLUSIONS

In this paper, we introduce a comprehensive enthalpy-based model that encompasses the solidification process of various materials. In this model, the effective and ineffective areas between different components are efficiently delineated using fractions. The heat transfer between different components is evaluated by comparing temperatures before and after sufficient mixing, and heat transfer between components is facilitated using a thermal source term. Compared with previous enthalpy-based models, this model successfully avoids the potential issue of transferring physical properties during the enthalpy distribution function transfer process.

(1) We have developed an enthalpy-based model for different materials. We use different forms of the enthalpy distribution function between different materials, still utilizing the enthalpy distribution function for collisions and streaming

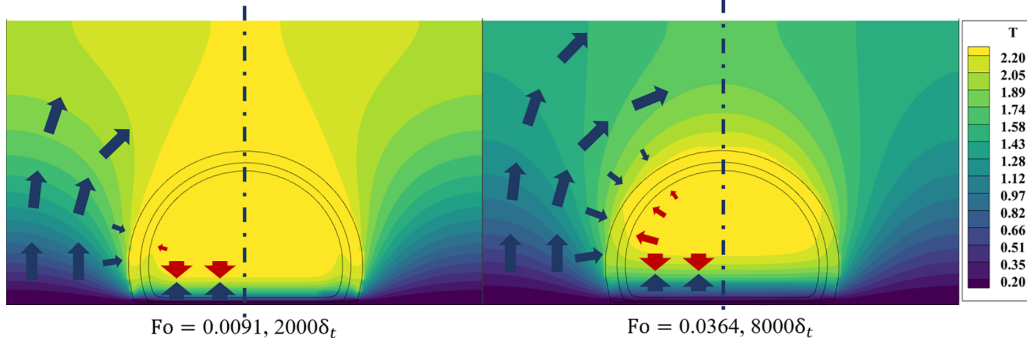


FIG. 8. In actual conditions ($\rho_l/\rho_g = 800$), the schematic diagram of the cold air enveloping the water droplet (dark blue arrows indicate cold transfer, red arrows indicate heat loss from the droplet).

processes among the same type of material. For different materials, instead of using the enthalpy distribution function form, the energy transfer between components is calculated

based on the temperature before and after sufficient mixing of different materials, and this is represented in the enthalpy distribution function equation of each component through a thermal source term.

(2) We have specifically applied the enthalpy-based model for different materials to the case of a water droplet solidifying in air, constructing an enthalpy-based model for two materials (water and air) and restoring the ratio of physical properties of air to water under actual conditions. The simulation results are in basic agreement with the experimental results. Additionally, the simulation demonstrates the significant difference in thermal diffusivity between water and air as well as the substantial disparity in heat transfer between them.

ACKNOWLEDGMENTS

This paper was supported by the National Science and Technology Major Project (Grant No. J2019-III-0017-0061), the National Natural Science Foundation of China (Grant No. U2241270), and by the Fundamental Research Funds for the Central Universities (Grant No. 3072024CFJ0303).

The authors declare that they have no known competing financial interests or personal relationships that could have appeared to influence the work reported in this paper.

APPENDIX

The experiment is primarily divided into four parts: droplet generation and control, temperature control, surface control, and image acquisition and analysis. The high-speed camera operates at a frame rate of 400 fps, while the infrared shooting frame rate is 100 fps. The experiment is conducted in an enclosed, insulated environment, with the room temperature set at 20 °C and the internal temperature of the experimental platform at 8 °C. The initial temperature of the droplet is 8.5 °C, with the low-temperature surface at −15 °C. The ambient temperature is measured by a temperature sensor, the droplet temperature is determined via infrared, and the surface temperature is obtained from the measured temperature of a frozen and stable droplet. The experimental surface, a regular smooth aluminum substrate cleaned with anhydrous ethanol, is either directly sprayed with NC319 hydrophobic coating or soaked in a 2% (heptadecafluoro-1,1,2,2-tetradecyl) trimethoxysilane ethanol solution to achieve a hydrophobic surface.

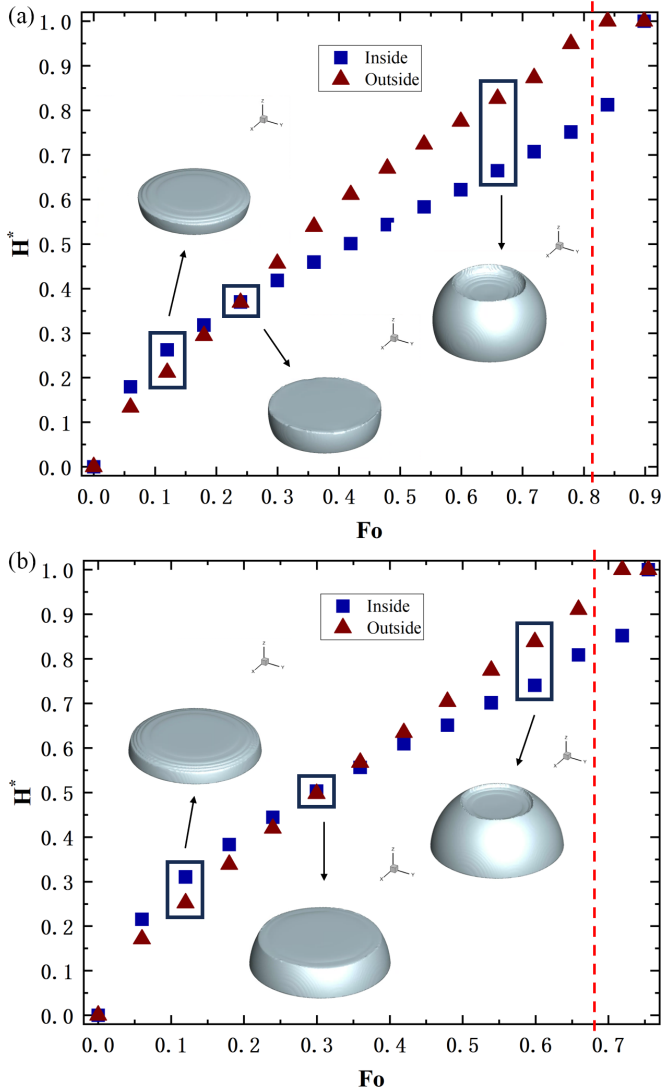


FIG. 9. Comparison of the growth peaks inside and outside the droplet (the red line distinguishes between areas that conform to and do not conform to experimental controls). (a) Contact angle $\theta = 103^\circ$. (b) Contact angle $\theta = 82^\circ$.

- [1] L. B. Boinovich and A. M. Emelyanenko, Anti-icing potential of superhydrophobic coatings, *Mendelev Commun.* **23**, 3 (2013).
- [2] M. J. Kreder, J. Alvarenga, P. Kim, and J. Aizenberg, Design of anti-icing surfaces: Smooth, textured or slippery? *Nat. Rev. Mater.* **1**, 15003 (2016).
- [3] L. Astráin-Redín, J. Abad, A. Rieder, B. Kirkhus, J. Raso, G. Cebrián, and I. Álvarez, Direct contact ultrasound assisted freezing of chicken breast samples, *Ultrason. Sonochem.* **70**, 105319 (2021).
- [4] H. Sojoudi, M. Wang, N. D. Boscher, G. H. McKinley, and K. K. Gleason, Durable and scalable icephobic surfaces: Similarities and distinctions from superhydrophobic surfaces, *Soft Matter* **12**, 1938 (2016).
- [5] T. M. Schutzius, S. Jung, T. Maitra, P. Eberle, C. Antonini, C. Stamatoopoulos, and D. Poulikakos, Physics of icing and rational design of surfaces with extraordinary icephobicity, *Langmuir* **31**, 4807 (2015).
- [6] H. Yang, M. Fu, Z. Zhan, R. Wang, and Y. Jiang, Study on combined freezing-based desalination processes with microwave treatment, *Desalination* **475**, 114201 (2020).
- [7] J. Resende de Azevedo, F. Espitalier, and M. I. Ré, Ultrasound assisted crystallization of a new cardioactive prototype using ionic liquid as solvent, *Ultrason. Sonochem.* **55**, 32 (2019).
- [8] S. Jung, M. Dorrestijn, D. Raps, A. Das, C. M. Megaridis, and D. Poulikakos, Are superhydrophobic surfaces best for icephobicity? *Langmuir* **27**, 3059 (2011).
- [9] G. Chaudhary and R. Li, Freezing of water droplets on solid surfaces: An experimental and numerical study, *Exp. Therm. Fluid Sci.* **57**, 86 (2014).
- [10] S. W. Han, J. Jeong, and D. H. Lee, Ice-phobic behavior of superhydrophobic Al surface under various etching conditions, *J. Electroceramics* **33**, 82 (2014).
- [11] G. Fang and A. Amirfazli, Understanding the anti-icing behavior of superhydrophobic surfaces, *Surf. Innov.* **2**, 94 (2014).
- [12] Y. Wang, L. Ju, D. Han, and Q. Wang, Numerical investigation of the impacting and freezing process of a single supercooled water droplet, *Phys. Fluids* **33**, 042114 (2021).
- [13] C. Zhang, H. Zhang, W. Fang, Y. Zhao, and C. Yang, Axisymmetric lattice Boltzmann model for simulating the freezing process of a sessile water droplet with volume change, *Phys. Rev. E* **101**, 023314 (2020).
- [14] M. Conti, U. M. B. Marconi, and A. Crisanti, A microscopic model for solidification, *EPL* **47**, 338 (1999).
- [15] A. Tiwari, R. Samanta, and H. Chattopadhyay, Droplet solidification: Physics and modelling, *Appl. Therm. Eng.* **228**, 120515 (2023).
- [16] X. Shan and H. Chen, Lattice Boltzmann model for simulating flows with multiple phases and components, *Phys. Rev. E* **47**, 1815 (1993).
- [17] X. Shan and H. Chen, Simulation of nonideal gases and liquid-gas phase transitions by the lattice Boltzmann equation, *Phys. Rev. E* **49**, 2941 (1994).
- [18] Q. Li, K. H. Luo, and X. J. Li, Forcing scheme in pseudopotential lattice Boltzmann model for multiphase flows, *Phys. Rev. E* **86**, 016709 (2012).
- [19] A. J. Wagner and C. M. Pooley, Interface width and bulk stability: Requirements for the simulation of deeply quenched liquid-gas systems, *Phys. Rev. E* **76**, 045702(R) (2007).
- [20] Q. Li, K. H. Luo, and X. J. Li, Lattice Boltzmann modeling of multiphase flows at large density ratio with an improved pseudopotential model, *Phys. Rev. E* **87**, 053301 (2013).
- [21] G. Wang, L. Fei, and K. H. Luo, Unified lattice Boltzmann method with improved schemes for multiphase flow simulation: Application to droplet dynamics under realistic conditions, *Phys. Rev. E* **105**, 045314 (2022).
- [22] L. Fei, J. Du, K. H. Luo, S. Succi, M. Lauricella, A. Montessori, and Q. Wang, Modeling realistic multiphase flows using a non-orthogonal multiple-relaxation-time lattice Boltzmann method, *Phys. Fluids* **31**, 042105 (2019).
- [23] Q. Li, P. Zhou, and H. J. Yan, Improved thermal lattice Boltzmann model for simulation of liquid-vapor phase change, *Phys. Rev. E* **96**, 063303 (2017).
- [24] Q. Li, Y. Yu, and K. H. Luo, Improved three-dimensional thermal multiphase lattice Boltzmann model for liquid-vapor phase change, *Phys. Rev. E* **105**, 025308 (2022).
- [25] Q. Li, Q. J. Kang, M. M. Francois, Y. L. He, and K. H. Luo, Lattice Boltzmann modeling of boiling heat transfer: The boiling curve and the effects of wettability, *Int. J. Heat Mass Transf.* **85**, 787 (2015).
- [26] W.-Z. Fang, L. Chen, Q.-J. Kang, and W.-Q. Tao, Lattice Boltzmann modeling of pool boiling with large liquid-gas density ratio, *Int. J. Therm. Sci.* **114**, 172 (2017).
- [27] L. Fei, J. Yang, Y. Chen, H. Mo, and K. H. Luo, Mesoscopic simulation of three-dimensional pool boiling based on a phase-change cascaded lattice Boltzmann method, *Phys. Fluids* **32**, 103312 (2020).
- [28] C. Zhang, P. Cheng, and W. J. Minkowycz, Lattice Boltzmann simulation of forced condensation flow on a horizontal cold surface in the presence of a non-condensable gas, *Int. J. Heat Mass Transf.* **115**, 500 (2017).
- [29] Y.-L. He, Q. Liu, Q. Li, and W.-Q. Tao, Lattice Boltzmann methods for single-phase and solid-liquid phase-change heat transfer in porous media: A review, *Int. J. Heat Mass Transf.* **129**, 160 (2019).
- [30] R. Huang and H. Wu, Phase interface effects in the total enthalpy-based lattice Boltzmann model for solid-liquid phase change, *J. Comput. Phys.* **294**, 346 (2015).
- [31] R. Huang and H. Wu, Total enthalpy-based lattice Boltzmann method with adaptive mesh refinement for solid-liquid phase change, *J. Comput. Phys.* **315**, 65 (2016).
- [32] D. Li, Z.-X. Tong, Q. Ren, Y.-L. He, and W.-Q. Tao, Three-dimensional lattice Boltzmann models for solid-liquid phase change, *Int. J. Heat Mass Transf.* **115**, 1334 (2017).
- [33] Q. Liu, X. Wang, X.-B. Feng, and F. Liu, An enthalpy-based cascaded lattice Boltzmann method for solid-liquid phase-change heat transfer, *Appl. Therm. Eng.* **209**, 118283 (2022).
- [34] W.-S. Jiaung, J.-R. Ho, and C.-P. Kuo, Lattice Boltzmann method for the heat conduction problem with phase change, *Numer. Heat Transf. B: Fundam.* **39**, 167 (2001).
- [35] C. Huber, A. Parmigiani, B. Chopard, M. Manga, and O. Bachmann, Lattice Boltzmann model for melting with natural convection, *Int. J. Heat Fluid Flow* **29**, 1469 (2008).
- [36] J. Sun, J. Gong, and G. Li, A lattice Boltzmann model for solidification of water droplet on cold flat plate, *Int. J. Refrig.* **59**, 53 (2015).
- [37] X. Zhao, B. Dong, W. Li, and B. Dou, An improved enthalpy-based lattice Boltzmann model for heat and mass transfer of the freezing process, *Appl. Therm. Eng.* **111**, 1477 (2017).

- [38] X. Li, J. Zhao, and P. Cheng, A lattice Boltzmann model for condensation and freezing of dry saturated vapor about a cryogenic spot on an inclined hydrophobic surface, *Int. J. Heat Mass Transf.* **114**, 628 (2017).
- [39] Y. Xu, L. Tian, Q. Bian, W. Guo, C. Zhu, and N. Zhao, Three-dimensional lattice Boltzmann simulations for droplet impact and freezing on ultra-cold superhydrophobic surfaces, *Phys. Fluids* **35**, 123321 (2023).
- [40] K. Luo, F.-J. Yao, H.-L. Yi, and H.-P. Tan, Lattice Boltzmann simulation of convection melting in complex heat storage systems filled with phase change materials, *Appl. Therm. Eng.* **86**, 238 (2015).
- [41] J. García Pérez, S. Leclaire, S. Ammar, J.-Y. Trépanier, M. Reggio, and A. Benmeddour, Investigations of water droplet impact and freezing on a cold substrate with the lattice Boltzmann method, *Int. J. Thermofluids* **12**, 100109 (2021).
- [42] P. Xu, S. Xu, Y. Gao, and P. Liu, A multicomponent multiphase enthalpy-based lattice Boltzmann method for droplet solidification on cold surface with different wettability, *Int. J. Heat Mass Transf.* **127**, 136 (2018).
- [43] Y. Zhao, G. G. Pereira, S. Kuang, Z. Chai, and B. Shi, A generalized lattice Boltzmann model for solid-liquid phase change with variable density and thermophysical properties, *Appl. Math. Lett.* **104**, 106250 (2020).
- [44] D. d'Humières, Generalized lattice-Boltzmann equations, in *Rarefied Gas Dynamics: Theory and Simulations*, Progress in Astronautics and Aeronautics, edited by B. D. Shizgal and D. P. Weaver (AIAA, Washington, DC, 1992), Vol. 159, pp. 450–458.
- [45] P. Lallemand and L.-S. Luo, Theory of the lattice Boltzmann method: Dispersion, dissipation, isotropy, Galilean invariance, and stability, *Phys. Rev. E* **61**, 6546 (2000).
- [46] Z. Chai and B. Shi, Multiple-relaxation-time lattice Boltzmann method for the Navier-Stokes and nonlinear convection-diffusion equations: Modeling, analysis, and elements, *Phys. Rev. E* **102**, 023306 (2020).
- [47] L. Fei and K. H. Luo, Cascaded lattice Boltzmann method for incompressible thermal flows with heat sources and general thermal boundary conditions, *Comput. Fluids* **165**, 89 (2018).
- [48] Q. Li, D. H. Du, L. L. Fei, and K. H. Luo, Three-dimensional non-orthogonal MRT pseudopotential lattice Boltzmann model for multiphase flows, *Comput. Fluids* **186**, 128 (2019).
- [49] Z. Guo, C. Zheng, and B. Shi, Discrete lattice effects on the forcing term in the lattice Boltzmann method, *Phys. Rev. E* **65**, 046308 (2002).
- [50] C. Chen, L. Li, R. Mei, and J. F. Klausner, Chapman-Enskog analyses on the gray lattice Boltzmann equation method for fluid flow in porous media, *J. Stat. Phys.* **171**, 493 (2018).
- [51] P. Yuan and L. Schaefer, Equations of state in a lattice Boltzmann model, *Phys. Fluids* **18**, 042101 (2006).
- [52] Q. Li and K. H. Luo, Thermodynamic consistency of the pseudopotential lattice Boltzmann model for simulating liquid-vapor flows, *Appl. Therm. Eng.* **72**, 56 (2014).
- [53] Q. Li and K. H. Luo, Achieving tunable surface tension in the pseudopotential lattice Boltzmann modeling of multiphase flows, *Phys. Rev. E* **88**, 053307 (2013).
- [54] K. H. Luo, L. Fei, and G. Wang, A unified lattice Boltzmann model and application to multiphase flows, *Phil. Trans. R. Soc. A* **379**, 20200397 (2021).
- [55] Z. Dai, J. Zhu, Z. Wang, S. Chu, and Y. Wang, Adaptive thermodynamic consistency control via interface thickness in pseudopotential lattice Boltzmann method across wide temperature ranges, *Phys. Fluids* **36**, 033349 (2024).
- [56] J. Yang, L. Fei, X. Zhang, X. Ma, K. H. Luo, and S. Shuai, Dynamic behavior of droplet transport on realistic gas diffusion layer with inertial effect via a unified lattice Boltzmann method, *Int. J. Hydrog. Energy* **46**, 33260 (2021).
- [57] Q. Li, Y. Yu, and K. H. Luo, Implementation of contact angles in pseudopotential lattice Boltzmann simulations with curved boundaries, *Phys. Rev. E* **100**, 053313 (2019).
- [58] L. Fei, K. H. Luo, C. Lin, and Q. Li, Modeling incompressible thermal flows using a central-moments-based lattice Boltzmann method, *Int. J. Heat Mass Transf.* **120**, 624 (2018).
- [59] Y. Guo, X. Zhang, X. Liu, X. Wu, and J. Min, Lattice Boltzmann simulation of droplet solidification processes with different solid-to-liquid density ratios, *Int. J. Therm. Sci.* **198**, 108881 (2024).